JOURNAL OF THERMOPHYSICS AND HEAT TRANSFER
Vol. 17, No. 1, January–March 2003

# Heat Transfer in High-Temperature Fibrous Insulation

Kamran Daryabeigi*
*NASA Langley Research Center, Hampton, Virginia 23681*

**The combined radiation/conduction heat transfer in high-porosity, high-temperature fibrous insulations was investigated experimentally and numerically. The effective thermal conductivity of fibrous insulation samples with densities of 24–72 kg/m$^3$ and thicknesses of 13.3–39.9 mm was measured over the temperature range of 300–1300 K and environmental pressure range of $1.33\times10^{-5}$–101.32 kPa. It was experimentally determined that for the fibrous insulation densities and thicknesses investigated no heat transfer takes place through natural convection. A finite volume numerical model was developed to solve the governing combined radiation and conduction heat-transfer equations. The radiation heat transfer was modeled using the modified two-flux approximation assuming anisotropic scattering and gray medium. A genetic-algorithm-based parameter estimation technique was used in conjunction with a subset of steady-state effective thermal conductivity measurements to determine the relevant conductive and radiative properties of the fibrous insulation. The numerical model was verified by comparison with steady-state effective thermal conductivity measurements and a transient thermal test simulating reentry aerodynamic heating conditions.**

## Nomenclature

| | | |
|---|---|---|
| $A$ | = | fraction of conduction heat transfer in parallel mode |
| $b$ | = | backscattering fraction |
| $c$ | = | specific heat, J/kg/K |
| $D_f$ | = | fiber diameter, m |
| $d_g$ | = | gas collision diameter, m |
| $e$ | = | specific extinction coefficient ($e = \beta/\rho$), m$^2$/kg |
| $F^+$ | = | forward radiative flux, W/m$^2$ |
| $F^-$ | = | backward radiative flux, W/m$^2$ |
| $f$ | = | solid fraction ratio |
| $K_B$ | = | Boltzmann constant, $1.3806\times10^{-23}$ J/K |
| $Kn$ | = | Knudsen number |
| $k$ | = | thermal conductivity, W/m/K |
| $L$ | = | insulation thickness, m |
| $L_c$ | = | characteristic length, m |
| $m$ | = | solid conduction exponent term |
| $n$ | = | index of refraction |
| $P$ | = | pressure, Pa |
| $Pr$ | = | Prandtl number |
| $q$ | = | heat flux, W/m$^2$ |
| $R$ | = | rms deviation |
| $S$ | = | sum of the squares of deviations |
| $T$ | = | temperature, K |
| $t$ | = | time, s |
| $x$ | = | spatial coordinate, m |
| $z$ | = | parameter for conduction heat-transfer model [Eq. (17e)] based on fiber orientation |
| $\alpha$ | = | thermal accommodation coefficient |
| $\beta$ | = | extinction coefficient, 1/m |
| $\gamma$ | = | specific heat ratio |
| $\varepsilon$ | = | emittance |
| $\eta$ | = | number of data points |
| $\lambda$ | = | molecular mean free path, m |
| $\xi$ | = | forward-scattering fraction |
| $\rho$ | = | density, kg/m$^3$ |
| $\sigma$ | = | Stefan-Boltzmann constant, $5.668\times10^{-8}$ W/m$^2$/K$^4$ |
| $\tau_0$ | = | optical thickness |
| $\omega$ | = | albedo of scattering |

*Subscripts*

| | | |
|---|---|---|
| $e$ | = | effective property |
| $e$-$m$ | = | measured effective property |
| $e$-$p$ | = | predicted effective property |
| $g$ | = | gas |
| $r$ | = | radiation |
| $s$ | = | solid |
| $T$ | = | total |

*Superscripts*

| | | |
|---|---|---|
| $*$ | = | property at atmospheric pressure |
| $**$ | = | property of parent material |

## Introduction

THE purpose of this work is to investigate heat transfer in high-porosity, high-temperature fibrous insulation subject to temperature and pressure conditions representative of reentry aerodynamic heating for reusable launch vehicles. The fibrous insulation considered in this study is loose fibrous insulation made of alumina that can be used in metallic thermal protection systems for reusable launch vehicles. The thermal protection system is used to maintain a reusable launch vehicle's structural temperature within acceptable limits during reentry flight. The space shuttle's thermal protection system consists of rigid fibrous insulation ceramic tiles and flexible blankets. Metallic thermal protection systems have been considered for the next generation of reusable launch vehicles.[1] A metallic thermal protection system consists of a metallic shell panel fabricated from a high-temperature metallic alloy and mechanically attached to the vehicle structure; the shell is filled with lightweight, non-load-bearing loose fibrous insulation.

Heat transfer through a fibrous insulation during atmospheric reentry involves combined modes of heat transfer: solid conduction through fibers, gas conduction in the void spaces between fibers, and radiation interchange through participating media in the fibrous insulation, and possibly natural convection depending on the orientation of the imposed heat flux and the gravity vector. The fibrous insulation is subjected to environmental pressures in the range of $1.33\times10^{-5}$–101.32 kPa, and temperatures in the range of 300–1300 K. Various formulations for heat transfer through fibrous

Received 20 June 2002; presented as Paper 2002-3332 at the AIAA/ASME 8th Joint Thermophysics and Heat Transfer Conference, St. Louis, MO, 24–27 June 2002; revision received 19 September 2002; accepted for publication 20 September 2002. 

*Aerospace Engineer, Metals and Thermal Structures Branch, Mail Stop 396. Senior Member AIAA.

insulation have been investigated, but most of the models have been validated with experimental results over only a limited pressure and temperature range. Lee and Cunnington[2] have provided an extensive review of the various analytical formulations used for modeling the radiation component of heat transfer through fibrous insulation. A brief review of some pertinent research is provided. Two distinctly different classes of solutions have been attempted.

In the first class of solutions, the researchers developed an effective thermal conductivity model based on superposition of gas, solid, and apparent radiation thermal conductivities, based on the optically thick assumption, and compared the results with measured effective thermal conductivities of samples subjected to small temperature differences across the insulation thicknesses. Verschoor and Greebler[3] used a gas conduction model valid from the rarefied to the continuum regime and validated their model by comparison with thermal conductivity measurements over a pressure range of 0.133–101.32 kPa and temperatures up to 340 K. Hager and Steere[4] neglected solid conduction and used an approximate gas conduction model and compared their results with experimental results at 300 K at a pressure range of $1.33 \times 10^{-7}$–101.32 kPa. Bankvall[5] provided a detailed model of the interaction between solid and gas thermal conductivities and compared his analysis with experimental results obtained at pressures of $1.33 \times 10^{-4}$–101.32 kPa and at temperatures up to 350 K. Pawel et al.[6] studied rigid insulation and used an effective thermal conductivity based on linear superposition of gas and solid conduction taking place both in parallel and series arrangements. They compared their predictions with experimental results for pressures between 5.332 and 101.32 kPa and temperatures up to 1200 K. Bhattacharyya[7] investigated various forms of combining solid and gaseous conduction modes.

In the second class of solutions, researchers calculated approximate analytical or numerical solutions for the heat transfer through insulations. Larkin and Churchill[8] used a two-flux approximation assuming a purely scattering medium to model radiation heat transfer and compared their results with measured optical transmission through fibrous insulation samples. Tong and Tien[9] and Tong et al.[10] modeled radiation heat transfer through fibrous insulations using the two-flux model assuming linear anisotropic scattering and compared their predicted total heat fluxes with measured data up to 450 K and at one atmosphere. In Ref. 11 an apparent radiant conductivity based on the diffusion approximation was used in a numerical solution of the combined conduction/radiation heat transfer in fibrous insulations and compared with effective thermal conductivity measurements over a temperature range of 300–1300 K and pressure range of $1.33 \times 10^{-5}$–101.32 kPa. In follow-on work the combined radiation/conduction heat transfer in fibrous insulation spacers between reflective foils of high-temperature multilayer insulations was modeled using the two-flux approximation assuming isotropic scattering for the radiation heat transfer.[12,13] Lee and Cunnington[2] computed the combined conduction radiation heat transfer in fibrous insulation using an optically thick assumption and anisotropic scattering and compared their predictions with published experimental results at temperatures up to 800 K and pressures up to 2 Pa.

Starke and Fricke[14] and Bhattacharyya[7] have stated that there is no natural convection in fibrous insulations with densities larger than 20 kg/m$^3$ because the fibers subdivide the gas into sufficiently small pores. Even though natural convection has generally been ignored as a possible mode of heat transfer in high-porosity fibrous insulations, Verschoor and Greebler[3] attributed the difference in measured and calculated heat transfer through insulations to natural convection heat transfer.

The objective of this investigation was to investigate experimentally whether natural convection is a mode of heat transfer in high-porosity fibrous insulations for thermal protection systems and model the heat transfer through fibrous insulation with a numerical model verified by both steady-state and transient thermal tests. The steady-state tests consisted of measuring the effective thermal conductivity of the fibrous insulation at various densities and thicknesses over an extended temperature and pressure range, 300–1300 K and $1.33 \times 10^{-5}$–101.32 kPa. The transient test consisted of subjecting a fibrous insulation sample to simulated reentry aerodynamic heating conditions in a thermal vacuum chamber. For the numerical model the radiation heat transfer was modeled using the modified two-flux method assuming anisotropic scattering. Various forms of modeling gas and solid conduction interaction were investigated. A genetic-algorithm-based parameter estimation technique was utilized to determine the relevant conductive and radiative properties of the fibrous insulation over the temperature range of 300–1300 K.

## Experimental Approach

Both steady-state and transient tests were used for studying the thermal behavior of fibrous insulations and for verifying the numerical heat-transfer model. A brief description of the fibrous insulation samples and the steady state and transient thermal testing apparatus is provided.

### Fibrous Insulation Samples

The fibrous insulation samples studied in this investigation utilized alumina fibers with a mean fiber strand diameter of $3 \times 10^{-6}$ m and a maximum operating temperature of 1900 K. For the present study 10 different fibrous insulation samples were tested. All of the samples consisted of randomly oriented fibers. A listing of the samples with their respective thicknesses, densities, solid fraction ratios (ratio of insulation density to density of alumina), type of testing, and heat source location relative to the sample is provided in Table 1. Nine samples were used in the steady-state thermal testing apparatus and had planform dimensions of $203.2 \times 203.2$ mm. The samples were 13.3, 26.6, and 39.9 mm thick. The fibrous insulation considered for the most recent metallic thermal protection system design[1] is at a density of 48 kg/m$^3$; therefore, test samples with densities of 0.5, 1, and 1.5 times this density were chosen, resulting in sample densities of 24, 48, and 72 kg/m$^3$. Furthermore, the samples were tested in two different heating orientations. For samples 1–7 heat was applied from the top, resulting in the heat-flux vector being aligned with the gravity vector. With this orientation there was no natural convection heat transfer in the sample. For samples 8 and 9 heat was applied from the bottom, resulting in the heat-flux vector being in the opposite direction of the gravity vector. This orientation was conducive to development of natural convection. Furthermore, samples 8 and 9 had the lowest insulation density, thus further enhancing the chance of development of natural convection. Samples 3 and 8 had the same thickness and density but had different heating orientations. Similarly samples 6 and 9 only differed in the heating orientations. Therefore, the comparison of their effective thermal conductivity would determine whether natural convection is a mode of heat transfer in fibrous insulation samples. Sample 10 was used in the transient thermal testing apparatus and had dimensions of $304.8 \times 304.8$ mm. It had a thickness of 53.3 mm and a density of 45.1 kg/m$^3$ and was heated transiently from the top.

### Steady-State Thermal Testing Apparatus

A thermal conductivity apparatus, described in detail in Refs. 13 and 15, was used to measure the steady-state effective thermal conductivity of the fibrous insulation samples. The apparatus used in this study followed the general guidelines from American Society

**Table 1 Listing of fibrous insulation samples**

| Sample number | Thickness, mm | Density, kg/m$^3$ | Solid fraction ratio | Test | Heat source location |
|---|---|---|---|---|---|
| 1 | 13.3 | 24.2 | 0.0073 | Steady state | Top |
| 2 | 13.3 | 48.6 | 0.0147 | Steady state | Top |
| 3 | 26.6 | 24.2 | 0.0073 | Steady state | Top |
| 4 | 26.6 | 48 | 0.0145 | Steady state | Top |
| 5 | 26.6 | 72 | 0.0218 | Steady state | Top |
| 6 | 39.9 | 24.2 | 0.0073 | Steady state | Top |
| 7 | 39.9 | 72 | 0.0218 | Steady state | Top |
| 8 | 26.6 | 24.2 | 0.0073 | Steady state | Bottom |
| 9 | 39.9 | 24.2 | 0.0073 | Steady state | Bottom |
| 10 | 53.3 | 45.1 | 0.0137 | Transient | Top |

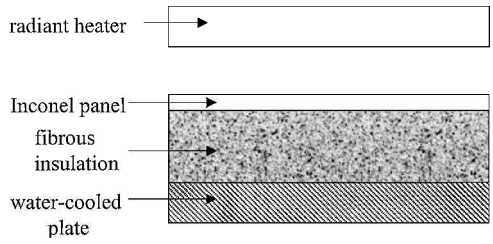


**Fig. 1 Schematic of thermal conductivity test apparatus (not to scale).**

for Testing and Materials (ASTM) standard C201 (Ref. 16). This test setup was not intended for measuring effective thermal conductivities of the test specimen subjected to small temperature differences maintained across the sample as is customary in the majority of steady-state thermal conductivity measurement techniques. The main purpose was to use a steady-state testing facility for characterization of the thermal performance of the insulation subject to pressures and temperature differences across the sample that would be representative of the conditions experienced during reentry aerodynamic heating conditions (environmental pressures range of $1.33 \times 10^{-5}$–101.32 kPa, with temperature differences as high as 1000 K maintained across the sample thickness). The results are presented as effective thermal conductivity, even though the results could have also been presented as total heat flux.

A schematic of the apparatus is shown in Fig. 1. The test specimen was located between a 6.4-mm-thick Inconel septum panel and a 25.4-mm-thick water-cooled aluminum plate, both plates having dimensions of $304.8 \times 304.8$ mm. The water-cooled plate was instrumented with nine thin-film heat-flux gauges and 10 type-K thermocouples, and the septum panel was instrumented with 23 metal-sheathed type-K thermocouples. The data from the thermocouples and heat-flux gauges from the central $127 \times 127$-mm section of the test setup were used for calculating effective thermal conductivities. Daryabeigi[15] provides details on the location of instrumentation on the water-cooled plate and septum plates. A ceramic radiant heater was used for heating and controlling the temperature of the septum plate. Refractory ceramic insulation boards 25.4-mm thick were placed around the apparatus to minimize heat losses (not shown in Fig. 1). The effective thermal conductivity of the sample was measured with septum panel temperature set at nominal temperatures between 373 and 1273 K and with the water-cooled plate maintained around room temperature. The apparatus was located inside a vacuum chamber, and the environmental pressure was varied between $1.33 \times 10^{-5}$ and 101.32 kPa. All of the tests were conducted in a gaseous nitrogen environment. Data were typically obtained with nominal temperature differences of 90, 260, 425, 590, 760, 870, and 980 K maintained across the sample thickness and with environmental pressures of $1.33 \times 10^{-5}$, $1.33 \times 10^{-4}$, $1.33 \times 10^{-3}$, $1.33 \times 10^{-2}$, 0.033, 0.066, 0.133, 0.333, 0.667, 1.33, 13.33, 99.99, and 101.32 kPa. Not all of the samples were tested at all of the nominal pressures and temperature differences. The effective thermal conductivity was calculated using Fourier's law of heat conduction using the following measured average parameters: septum panel temperature $T_1$, water-cooled plate temperature $T_2$, and heat flux $q$, according to

$$k_e = qL/(T_1 - T_2) \tag{1}$$

The orientation shown schematically in Fig. 1 was used for testing samples 1–7. For this orientation the heater was located on top of the test sample; therefore, the heat-flux vector was aligned with local gravity vector, and natural convection was not a mode of heat transfer. To investigate natural convection, the arrangement of the various components in the apparatus was reversed, thus resulting in the heater being at the bottom of the stackup. For this orientation the heat-flux vector was in the opposite direction of the gravity vector, thus being favorable to development of natural convection as a mode of heat transfer.

The average uncertainty of the effective thermal conductivity measurements was 7.5% over the entire range of pressures and temperatures (details of the uncertainty analysis are provided in Ref. 13). Measurements on a fumed silica board, Standard Reference Material 1459 from the National Institute of Standard and Technology, at temperatures up to 573 K were within 5.5% of published data.[11,13]

### Transient Thermal Testing Apparatus

A transient thermal test was conducted to simulate reentry aerodynamic heating conditions. The steady-state thermal conductivity apparatus was modified in order to perform the transient thermal test. The heater was changed from a ceramic radiant heater to a low thermal-mass quartz lamp radiant heating array in order to be able to provide the rapid changes in heating required for simulating the transient reentry heating profile. Furthermore, a $304.8 \times 304.8 \times 3.18$-mm aluminum panel instrumented with seven type-K thermocouples was installed in the stackup between the Inconel panel and the water-cooled plate.[13] A schematic of the transient thermal test apparatus is shown in Fig. 2. The test article (sample 10), a 53.3-mm-thick fibrous insulation sample with a density of 45.1 kg/m$^3$, was placed between the Inconel and aluminum panels. The Inconel panel served as the hot-side solid boundary, whereas the aluminum panel represented the launch vehicle structure. A 13.3-mm-thick alumina fibrous insulation with a density of 24.3 kg/m$^3$ was placed between the aluminum panel and the water-cooled plate to represent a heat loss mechanism from the launch vehicle structure attached to the thermal protection system. Typical reentry vehicle design assumes that the launch vehicle structure is adiabatic, but this assumption has been shown to be very conservative.[17,18] Furthermore, it is extremely difficult to maintain an adiabatic boundary condition; any insulation will conduct and absorb some heat. The present apparatus overcomes this difficulty. The measured transient temperatures of the Inconel septum panel and water-cooled plate can be used as boundary conditions in the numerical model, and then the comparison of the measured and numerically predicted aluminum panel temperature can be used for verification of the numerical model.

Refractory ceramic board insulation spacers having planform dimensions of $38.1 \times 38.1$ mm were used at the four corners of the test setup between the water-cooled plate and aluminum panel and between the aluminum and Inconel panels. These spacers were used to maintain the desired thickness of the insulation samples: 13.3 and 53.3 mm below and above the aluminum panel, respectively. Refractory ceramic insulation boards (not shown in Fig. 2), 25.4 mm thick, were placed around the apparatus to minimize heat losses.

The flight trajectory of the NASA winged-body reference vehicle configuration designated 001 (Ref. 19) was used in this study. A plot of the corresponding reentry flight profile is provided in Fig. 3, where the vehicle reentry altitude and velocity histories are shown. The surface pressure and heating rate histories for a location 5.1 m downstream of the nose cap on the centerline of the windward side of this vehicle were calculated[19] using MINIVER,[20] an engineering code used to estimate the aerothermal environment of entry vehicles. The corresponding radiation equilibrium temperatures[21] were calculated from the heating rates. A plot of the calculated radiative equilibrium temperature and surface pressure histories is shown in Fig. 4. For the transient thermal tests the Inconel panel's temperature

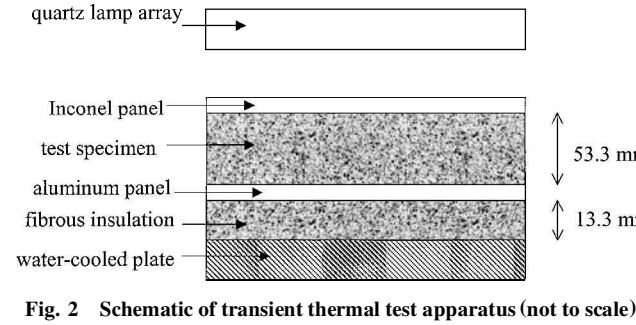


**Fig. 2 Schematic of transient thermal test apparatus (not to scale).**

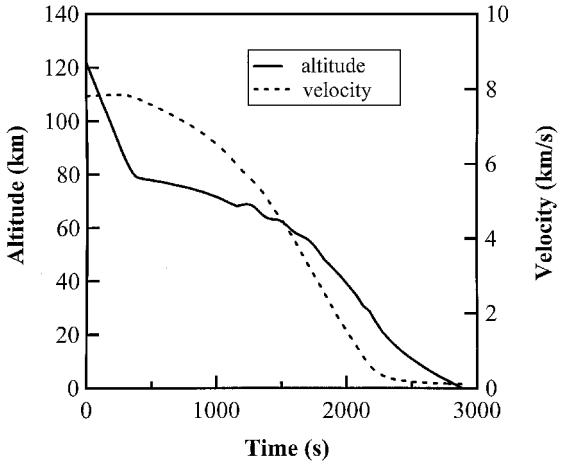


**Fig. 3 Reentry flight altitude and velocity profiles.**

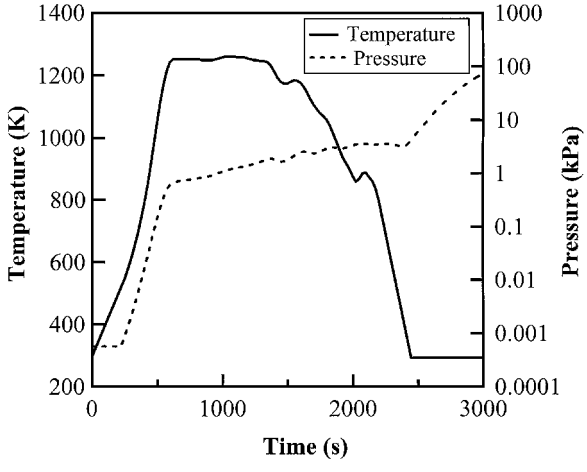


**Fig. 4 Reentry flight pressure and radiation equilibrium temperature profiles.**

was controlled to simulate the calculated trajectory transient radiative equilibrium temperatures, while the pressure in the vacuum chamber was varied in order to simulate the calculated trajectory surface pressures. The transient thermal test was conducted in a gaseous nitrogen environment. A more detailed description of the transient thermal testing apparatus is provided in Ref. 13.

## Analytical Model Development

In the absence of natural convection, the governing conservation of energy equation for the problem of combined radiation and conduction in a radiation participating medium bounded by two solid surfaces at specified temperatures is given by[22]

$$\rho c\frac{\partial T}{\partial t}=\frac{\partial}{\partial x}\left(k\frac{\partial T}{\partial x}\right)-\frac{\partial q_r}{\partial x} \tag{2}$$

subject to the following initial and boundary conditions:

$$T(x,0)=T_0(x) \tag{3}$$

$$T(0,t)=T_1(t) \tag{4a}$$

$$T(L,t)=T_2(t) \tag{4b}$$

Here $T_0$ is the initial temperature, and $T_1$ and $T_2$ are the transient specified temperatures on the boundaries.

The modified two-flux approximation was used for modeling the radiation heat transfer in the participating medium because the uncertainty in radiative properties over the temperature range of interest did not warrant use of more detailed models. Furthermore, even though typical fibrous insulations for thermal protection systems are of such thickness to be optically thick, the goal of the present study was to develop a model that can be used for both optically thick fibrous insulations and for very thin fibrous insulation spacers used in high-temperature multilayer insulations[12] that do not fall in the optically thick category. Assuming a gray medium in the modified two-flux approximation, the radiant flux is assumed to be composed of the forward and backward radiative fluxes:

$$q_r=F^+-F^- \tag{5}$$

where the forward and backward radiative fluxes are governed by

$$\frac{1}{\sqrt{3}\beta}\frac{\partial F^+}{\partial x}=-[1-\omega(1-b)]F^++b\omega F^-+(1-\omega)n^2\sigma T^4 \tag{6a}$$

$$-\frac{1}{\sqrt{3}\beta}\frac{\partial F^-}{\partial x}=-[1-\omega(1-b)]F^-+b\omega F^++(1-\omega)n^2\sigma T^4 \tag{6b}$$

This formulation assumes anisotropic scattering and has been used by Domoto and Wang[23] for radiative transfer in gases with nonisotropic particle scattering and by Matthews et al.[24] for solving the combined conduction and radiation heat transfer in porous materials. Assuming that the bounding solid surfaces are diffuse emitting/reflecting surfaces, the radiant boundary conditions are

$$F^+(0)=\varepsilon_1 n^2\sigma T_1^4+(1-\varepsilon_1)F^-(0) \tag{7a}$$

$$F^-(L)=\varepsilon_2 n^2\sigma T_2^4+(1-\varepsilon_2)F^+(L) \tag{7b}$$

where the subscripts 1 and 2 refer to the bounding surfaces at $x=0$ and $L$, respectively. The governing equations and boundary conditions given in Eqs. (6) and (7) constitute a system of first-order differential equations. Manipulation of Eqs. (6) and (7) to eliminate $F^-$ yielded the following second-order differential equation and boundary conditions for the forward radiative flux:

$$\frac{\partial^2 F^+}{\partial x^2}=3\beta^2\{[1-\omega(1-b)]^2-b^2\omega^2\}F^+-3\beta^2(1-\omega)$$
$$\times[1-\omega(1-2b)]n^2\sigma T^4+4\sqrt{3}\beta(1-\omega)n^2\sigma T^3\frac{\partial T}{\partial x} \tag{8a}$$

$$\frac{1}{\sqrt{3}\beta}\frac{\partial F^+}{\partial x}+\left[1-\omega(1-b)-\frac{b\omega}{1-\varepsilon_1}\right]F^+$$
$$=n^2\sigma T_1^4\left(1-\omega-\frac{\varepsilon_1 b\omega}{1-\varepsilon_1}\right) \tag{8b}$$

$$\frac{1}{\sqrt{3}\beta}\frac{\partial F^+}{\partial x}+[1-\omega(1-b)-b\omega(1-\varepsilon_2)]F^+$$
$$=n^2\sigma T_2^4(1-\omega+b\omega\varepsilon_2) \tag{8c}$$

where Eqs. (8b) and (8c) are applicable at $x=0$ and $L$, respectively. Once the distribution of the forward radiative flux is obtained from solving the preceding equations, the backward radiative flux is obtained from

$$F^-=\frac{1}{b\omega}\left\{\frac{1}{\sqrt{3}\beta}\frac{\partial F^+}{\partial x}+[1-\omega(1-b)]F^+-(1-\omega)n^2\sigma T^4\right\} \tag{9}$$

The extinction coefficient is related to the specific extinction coefficient through[25]

$$\beta=e\rho \tag{10}$$

whereas the optical thickness is related to the extinction coefficient through[22]

$$\tau_0 = \beta L \tag{11}$$

The albedo of scattering $\omega$, specific extinction coefficient $e$, and the backscattering fraction $b$ were not known and were determined using the parameter estimation technique described subsequently. The index of refraction $n$ was assumed to be unity. This assumption was also used by Marschall et al.[26] in analyzing radiation transport through rigid ceramic insulations by speculating that in a high-porosity medium the effective index of refraction should be dominated by the index of refraction of the void space.

Gas thermal conductivity does not vary with pressure, but the exchange of heat from gas molecules to bounding solid surfaces is influenced by the environmental pressure in the rarefied and transition flow transport regimes. Thus, an effective gas thermal conductivity was defined as[27]

$$k_g = k_g^* \Big/ \{\Phi + 2\Psi[(2-\alpha)/\alpha][2\gamma/(\gamma+1)](1/Pr)Kn\} \tag{12}$$

which relates the effective gas thermal conductivity at various pressures to the gas thermal conductivity at atmospheric pressure $k_g^*$. The parameters $\Phi$ and $\Psi$ depend on the Knudsen number. $\Phi = 1$, $\Psi = 0$ for Knudsen number less than 0.01 (continuum regime); $\Phi = 1$, $\Psi = 1$ for Knudsen number between 0.01 and 10 (transition regime); and $\Phi = 0$, $\Psi = 1$ for Knudsen number greater than 10 (free-molecular regime). The thermal accommodation coefficient for interchange between nitrogen gas and alumina fibers was assumed to be unity. The Knudsen number $Kn$ is calculated from[27]

$$Kn = \lambda / L_c \tag{13}$$

The gas molecular mean free path $\lambda$ is given by[28]

$$\lambda = \frac{K_B T}{\sqrt{2}\pi d_g^2 P} \tag{14}$$

The characteristic length $L_c$ for gas conduction in fibers having a diameter $D_f$ is defined as[3]

$$L_c = (\pi/4)(D_f/f) \tag{15}$$

The solid fraction ratio $f$ is defined as the ratio of density of fibrous insulation to the density of fiber parent material (alumina).

Theoretical modeling of solid conduction through fibers and points of contact between them is difficult, and various empirical relations have been developed to model the solid conduction. The empirical model used in this study was

$$k_s = f^m k_s^{**} \tag{16}$$

which relates the solid thermal conductivity of fibrous insulation to the thermal conductivity of the fiber parent material (alumina) $k_s^{**}$. This model is based on the model proposed by Verschoor and Greebler.[3] The exponent value $m$ of two was previously utilized for modeling solid conduction in fibrous insulation spacers in high-temperature multilayer insulations,[12] but for the present investigation it was decided to estimate the value of the exponent using parameter estimation techniques in order to better fit the data instead of arbitrarily setting it at two.

Different ways of modeling the interaction between solid and gas conduction have been used by various researchers. The parallel thermal network model has been used for modeling heat transfer in rigid[28] and loose fibrous insulations[12]:

$$k = fk_s + (1-f)k_g \tag{17a}$$

A combined parallel-series thermal network has also been used in rigid[6] and loose fibrous insulations[11]:

$$k = A[fk_s + (1-f)k_g] + (1-A)\left[\frac{k_s k_g}{(1-f)k_s + fk_g}\right] \tag{17b}$$

where $A$ and $(1-A)$ are the fractions of heat transfer in parallel and series mode, respectively. Lee and Cunnington have used the following formulation for rigid fibrous insulation[2]:

$$k = f\rho_s^m k_s + k_g \tag{17c}$$

Hager and Steere used a combination of solid conduction with a series thermal network for gas/solid conduction[4]:

$$k = 4f^3 k_s + \frac{k_s k_g}{(1-f)k_s + fk_g} \tag{17d}$$

Bhattacharyya developed a different model for combining solid and gas conduction[7]:

$$k = k_s + \frac{k_g - k_s}{1 + [f/(1-f)]\{1 + z[(k_g - k_s)/(k_g + k_s)]\}} \tag{17e}$$

with $z = 1$ when all of the fibers are perpendicular to the direction of heat flow, $z = \frac{2}{3}$ for random fiber orientation, and $z = \frac{5}{6}$ for half of fibers being random and the other half being normal to the direction of heat flow.

The criteria used for deciding which form to use for modeling the gas/solid conduction interaction were that the model should be dimensionally consistent and should reduce to $k_s^{**}$ when $f = 1$ and to $k_g$ when $f = 0$. The only two models that could meet these criteria were the parallel model [Eq. (17a)] and Bhattacharyya's model [Eq. (17e)], with the solid conduction term defined in Eq. (16). These two models were evaluated in this study.

The finite volume form of the conservation of energy equation, Eq. (2), was solved using an explicit time-marching formulation. Constant temperature boundary conditions were used for specifying data from the steady-state thermal conductivity measurements, whereas temporally varying boundary conditions were used for specifying the data from the transient thermal test. At each time step the governing equation and boundary conditions for the forward radiative flux, Eqs. (8a–8c), were solved using a finite difference technique using the predicted temperature distribution in the medium from the previous time-step solution of conservation of energy equation. The backward radiative flux distribution was then obtained from Eq. (9). Second-order finite difference approximations were used for the first-order derivatives in Eqs. (8) and (9). The radiant flux calculated from Eq. (5) was then used in Eq. (2) to obtain temperature distributions for the following time step. The conservation of energy equation [Eq. (2)] was solved using both Eqs. (17a) and (17e) for the combined thermal conductivity with the solid and gaseous thermal conductivities obtained from Eqs. (16) and (12), respectively. All of the thermophysical properties required for the numerical solution were obtained from published data in the literature, with the exception of the conduction and radiation parameters ($m$, $b$, $\omega$, $e$) that were estimated using genetic algorithm parameter estimation technique to be described in the following section. For modeling the steady-state test results the physical domain was discretized using 161, 321, and 481 nodes for sample thicknesses of 13.3, 26.6, and 39.9 mm, respectively. For modeling the transient test results 160 nodes were used in the 53.3-mm-thick fibrous insulation sample located between the septum and aluminum panels, whereas 40 nodes were used in the 13.3-mm-thick fibrous insulation sample located between the aluminum panel and the water-cooled plate. To study the adequacy of the numerical model mesh, the total number of nodes was doubled for the single case of simulating transient thermal test results. The difference between the predictions of aluminum panel temperature using the two different nodal spacings was less then 0.1 K.

## Parameter Estimation

The specific extinction coefficient, albedo of scattering, backscattering fraction, and the solid conduction exponent term were not known and were estimated using parameter estimation techniques. The estimation strategy was based on least-squares minimization of

the difference between measured and numerically predicted effective thermal conductivities for the fibrous insulation samples with a density of 24 kg/m$^3$ and at environmental pressures of $1.33 \times 10^{-4}$ and 99.98 kPa:

$$S = \sum_{i=1}^{\eta} [k_{e\text{-}m}(i) - k_{e\text{-}p}(i, e, \omega, b, m)]^2 \tag{18}$$

subject to the following physical constraints:

$$e \geq 0 \tag{19a}$$

$$0 \leq b \leq 1 \tag{19b}$$

$$0 \leq \omega \leq 1 \tag{19c}$$

The total number of samples used in the parameter estimation routine $\eta$ was 36. It was assumed that the albedo of scattering and backscattering fraction are independent of temperature, whereas the specific extinction coefficient was a linear function of temperature:

$$e = e_0 + e_1 T \tag{20}$$

Therefore a total of five parameters ($m$, $b$, $\omega$, $e_0$, $e_1$) needed to be estimated.

The genetic-algorithm optimization routine was used in conjunction with the numerical solution of the governing heat transfer equations for finding the set of parameters that minimized the objective function in Eq. (18), subject to the constraints provided in Eqs. (19a–19c). Genetic-algorithm optimization is a non-gradient-based optimization method that is built upon natural selection mechanisms and is described in detail elsewhere.[29,30]

## Results and Discussion

Typical steady-state thermal conductivity measurements are discussed. The thermal conductivity data with the two heating orientations for studying natural convection are presented. The results of the genetic-algorithm parameter estimation are discussed. The comparison of predicted and measured thermal conductivity data and the transient test results are presented.

### Steady-State Test Results

The effective thermal conductivity of fibrous insulation samples 1–7 as a function of temperature difference across the samples for an environmental pressure of $1.33 \times 10^{-4}$ kPa is shown in Fig. 5. Error bars representing the average overall uncertainty of ±7.5% are shown for the 26.6-mm-thick samples with densities of 24 and 48 kg/m$^3$. At this pressure gas conduction was negligible; therefore, the effective thermal conductivity comprised of contributions from solid conduction and radiation heat transfer. The effective thermal conductivity varied nonlinearly with temperature difference across

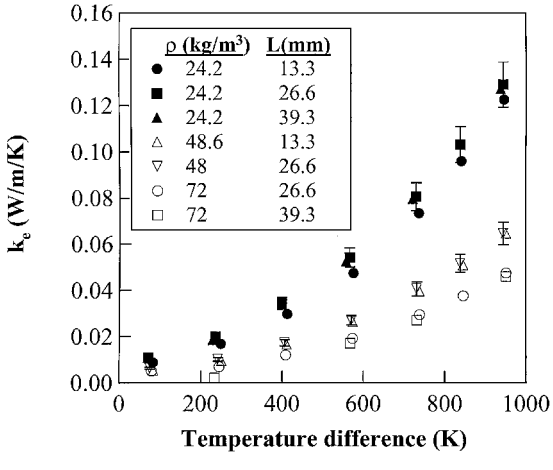


**Fig. 5 Variation of effective thermal conductivity with temperature difference across sample thickness at $P = 1.33 \times 10^{-4}$ kPa.**

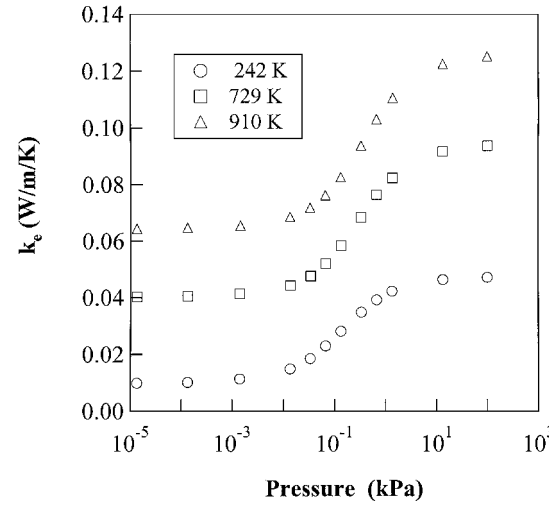


**Fig. 6 Variation of effective thermal conductivity with pressure at three temperature differences across the sample for $\rho$ = 48 kg/m$^3$ and $L$ = 26.6 mm.**

the sample, increasing rapidly with increasing temperature caused by the nonlinear radiation heat transfer. This effect was more pronounced with the lower density insulation, where radiation heat transfer was more dominant. The effective thermal conductivity decreased with increasing insulation density. As the density increased, the solid conduction contribution increased, but the radiation heat transfer decreased more rapidly, resulting in a net decrease in the effective thermal conductivity. Furthermore, the effective thermal conductivity does not appear to vary with sample thickness to within the experimental uncertainty range.

The variation of effective thermal conductivity with environmental pressure for fibrous insulation sample with density of 48 kg/m$^3$ and thickness of 26.6 mm is shown in Fig. 6. Data are plotted for three different nominal temperature differences across the sample: 240, 730, and 940 K. The measured effective thermal conductivity increases with increasing pressure. Gas conduction is almost negligible below $1.33 \times 10^{-4}$ kPa, where the gas is in a free molecular rarefied state. Gas conduction rapidly increases between $1.33 \times 10^{-2}$ and 1.33 kPa, where the gas goes through a transition region between free molecular and continuum states and then stays relatively constant between 13.33 and 101.32 kPa, where the gas is in a continuum state. The same trends were observed in all of the other samples.

### Natural Convection

The variation of effective thermal conductivity with the applied heating orientation, aligned or opposite to gravity, for insulation samples with a density of 24 kg/m$^3$ and thicknesses of 26.6 and 39.9 mm, is shown in Figs. 7a and 7b, respectively. Data are plotted as effective thermal conductivity vs temperature difference across the sample for environmental pressures of 0.133 and 99.99 kPa. If natural convection is a feasible mode of heat transfer in these fibrous insulations, it should manifest itself in the data with the applied heating opposite to the gravity vector and should result in higher effective thermal conductivities compared to tests with the applied heating aligned with the gravity vector. Furthermore, natural convection is more likely to occur at the insulation density of 24 kg/m$^3$, which is the lowest density and highest porosity sample tested in the present study. The data in Figs. 7a and 7b indicate that within the experimental uncertainty range (±7.5%) there is no difference between measurements at the two orientations, even at a 1000 K temperature difference maintained across the sample thickness. This observation verifies that natural convection is not a mode of heat transfer for fibrous insulation samples with densities equal to or greater than 24 kg/m$^3$.

### Verification of Numerical Model: Steady-State Results

For simulating steady-state thermal tests a linearly varying initial temperature distribution was assumed throughout the insulation

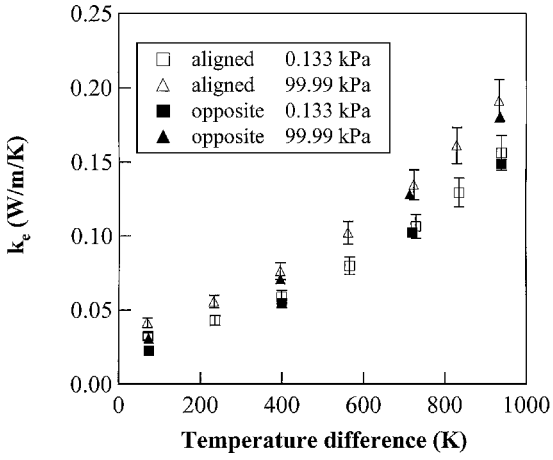


a) $L$ = 26.6 mm

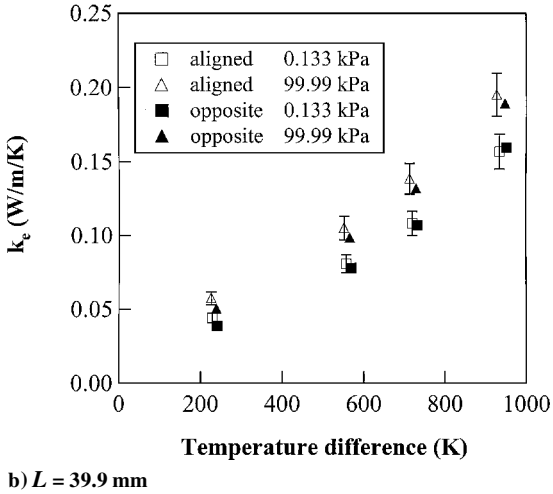


b) $L$ = 39.9 mm

**Fig. 7 Variation of effective thermal conductivity at two pressures and sample orientations with respect to gravity for $\rho$ = 24 kg/m$^3$.**

thickness between the measured hot and cold side temperatures. The solution of the transient conservation of energy equation was marched in time until a steady-state condition was achieved, and then the effective thermal conductivity was calculated from the Fourier's law of heat conduction using the calculated total steady-state heat flux (including contributions of both radiative and conductive heat fluxes) and the imposed temperature difference across the medium according to Eq. (1).

The genetic-algorithm parameter estimation technique was utilized in conjunction with the numerical solution of the governing heat-transfer equations to estimate the radiation and conduction parameters needed ($m$, $b$, $\omega$, $e_0$, $e_1$). Parameter estimation was conducted using both the parallel network model [Eq. (17a)] and Bhattacharyya's model [Eq. (17e)] with $z = \frac{5}{6}$ for modeling gas/solid conduction interaction. The parameter estimation was based on minimizing the sum of the square of differences between measured and numerically predicted effective thermal conductivities for fibrous insulation data with a density of 24 kg/m$^3$. Data at pressures of $1.33 \times 10^{-4}$ and 99.98 kPa, at three sample thicknesses of 13.3, 26.6, and 39.9 mm, and various temperature differences (7, 7, and 4 temperature differences for sample thicknesses of 13.3, 26.6, and 39.9 mm, respectively) were used, resulting in a total of 36 data points. The estimated radiative and conductive parameters are independent of insulation density and thickness; therefore, any subset of data (various densities and thicknesses) could have been used in the parameter estimation. It was decided to use the data with a density of 24 kg/m$^3$ because the ratio of radiation to conduction heat transfer is higher at this lower insulation density, thus providing a higher sensitivity for estimating the radiative properties. The results of the parameter estimation for both models for modeling gas/solid conduction interaction are presented in Table 2. The parameters, the sum of the square of differences $S$, and the rms deviation $R$ are presented. The rms deviation is obtained from

$$R = \sqrt{S/\eta} \tag{21}$$

Two rms deviations are presented in Table 2. $R_1$ is for the samples used in the parameter estimation (36 data points), whereas $R_2$ is for all of the data points used in the study including the data points used in the parameter estimation (443 data points). $R_1$ is indicative of how good a fit has been obtained for data with a density of 24 kg/m$^3$ and at pressures of $1.33 \times 10^{-4}$ and 99.98 kPa, whereas $R_2$ is indicative of how good the model and estimated parameters apply over all densities, pressures, and temperature differences. Both solid/gas conduction interaction models yielded similar results with Bhattacharyya's model [Eq. (17e)] yielding slightly better results based on the tabulated rms deviations. The results indicate that the alumina fibrous insulation evaluated in this study is highly scattering ($\omega \geq 0.97$) and strongly forward scattering ($\xi = 1 - b \geq 0.72$). Matthews et al.[24] estimated an albedo of scattering of 0.99 with a backscattering fraction of 0.2506 for zirconia rigid insulation, whereas Tong and Tien[9] had theoretically predicted an albedo of scattering of 0.68 with a backscattering fraction of 0.379 for silica fibrous insulation with mean fiber strand diameter of $5 \times 10^{-6}$ m.

Using thermophysical properties from published data in the literature and the conduction and radiation parameters listed in Table 2, the predicted effective thermal conductivities of the fibrous insulation samples calculated from the numerical solution of the conservation of energy equation were compared with the measured effective thermal conductivities. The numerical solutions were obtained using both gas/solid conduction interaction models [Eqs. (17a) and (17e)]. The comparison of measured and predicted effective thermal conductivities for the 13.3-mm-thick sample with a density of 24.2 kg/m$^3$ is provided in Fig. 8. Data are presented as effective thermal conductivity vs pressure for temperature differences

**Table 2 Parameter estimation results**

| Parameters and results | Gas/solid conduction interaction model: Parallel model, Eq. (17a) | Gas/solid conduction interaction model: Bhattacharyya's model,[7] Eq. (17e) |
|---|---|---|
| $\omega$ | 0.974 | 0.988 |
| $b$ | 0.268 | 0.272 |
| $e_0$ | 53.017 | 53.158 |
| $e_1$ | $3.879 \times 10^{-2}$ | $3.883 \times 10^{-2}$ |
| $m$ | 1.469 | 1.439 |
| $S$ | $9.21 \times 10^{-4}$ | $9.15 \times 10^{-4}$ |
| $R_1$ | $5.057 \times 10^{-3}$ | $5.042 \times 10^{-3}$ |
| $R_2$ | $3.616 \times 10^{-3}$ | $3.462 \times 10^{-3}$ |

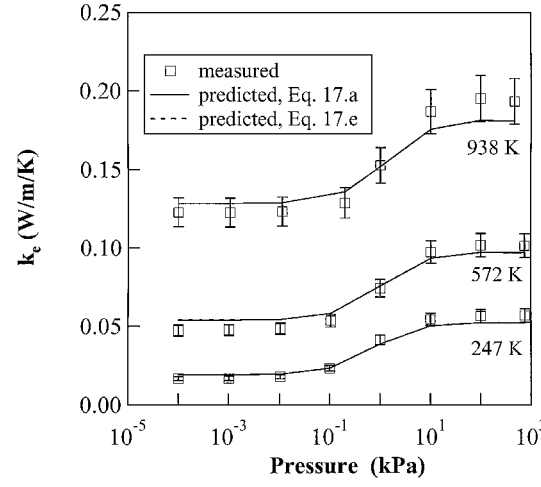


**Fig. 8 Comparison of predicted and measured effective thermal conductivity using two solid/gas combined thermal conductivity models for $\rho$ = 24.2 kg/m$^3$, $L$ = 13.3 mm.**

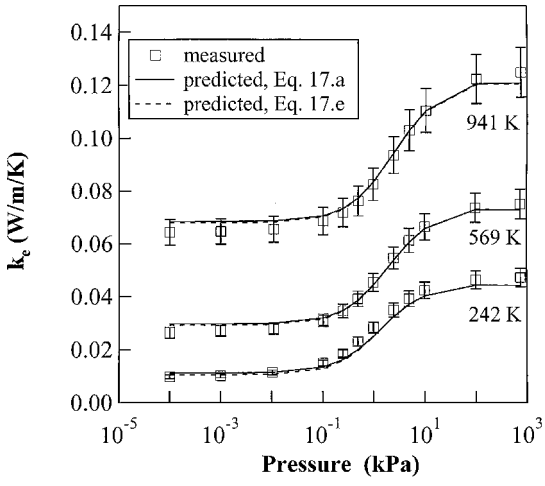


**Fig. 9 Comparison of predicted and measured effective thermal conductivity using two solid/gas combined thermal conductivity models for $\rho = 48$ kg/m$^3$, $L = 26.6$ mm.**

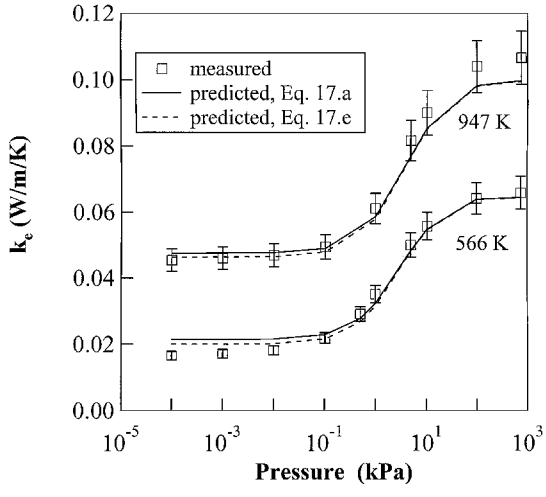


**Fig. 10 Comparison of predicted and measured effective thermal conductivity using two solid/gas combined thermal conductivity models for $\rho = 72$ kg/m$^3$, $L = 39.9$ mm.**

of 247, 572, and 938 K maintained across the sample thickness. It should be noted that the numerical data were forced to fit the experimental data at the extreme high-and low-pressure points for this insulation density using the genetic algorithm parameter estimation. The numerical data using the two different gas/solid conduction interaction models [Eqs. (17a) and (17e)] almost coincide and are not discernible in the figure and generally match the experimental measurements to within the ±7.5% experimental uncertainty. The comparison of measured and predicted effective thermal conductivities for the 26.6-mm-thick sample with a density of 48 kg/m$^3$ for temperature differences of 242, 569, and 941 K maintained across the sample thickness is provided in Fig. 9. Figure 10 shows the comparison of measured and predicted effective thermal conductivities for the 39.9-mm-thick sample with a density of 72 kg/m$^3$ and for temperature differences of 566 and 947 K maintained across the sample thickness. The predictions using both gas/solid interaction models for both insulation densities and at the thicknesses shown in Figs. 9 and 10 generally coincided with each other and matched the experimental data to within the ±7.5% experimental uncertainty. Because no data from the measurements with densities of 48 and 72 kg/m$^3$ were used in the parameter estimation technique, the good agreement between the predicted and measured data indicates that the approximate formulations used in the study have produced satisfactory results.

To study the relative significance of radiative and conductive heat fluxes throughout the insulation thickness, the numerical model

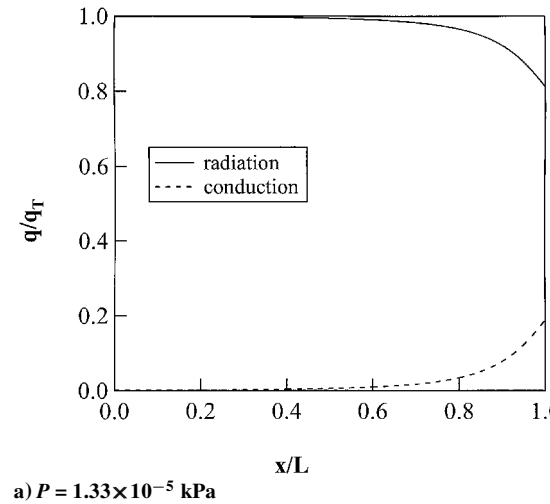


a) $P = 1.33 \times 10^{-5}$ kPa

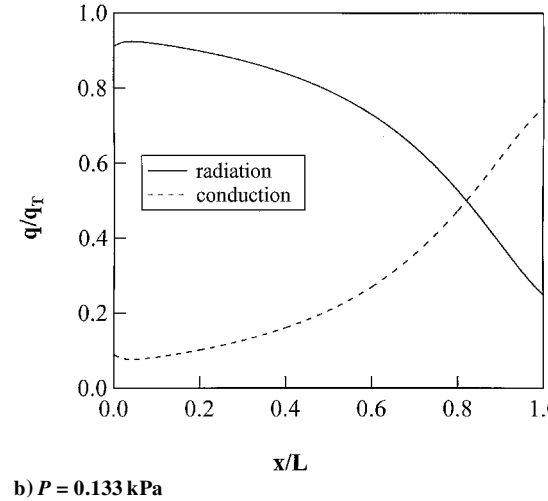


b) $P = 0.133$ kPa

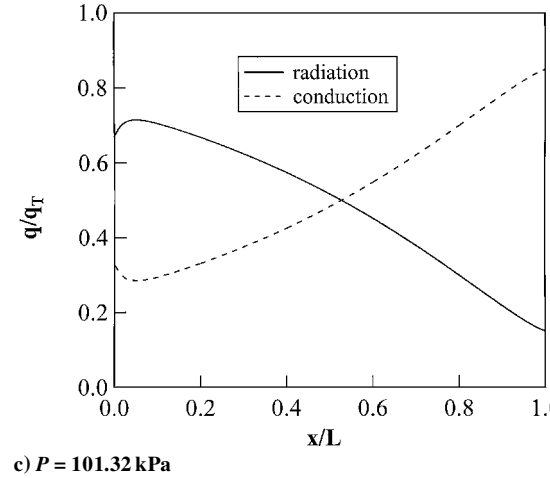


c) $P = 101.32$ kPa

**Fig. 11 Spatial variation of ratio of conduction and radiation fluxes to total heat flux ($\Delta T = 1000$ K, $\rho = 48$ kg/m$^3$, $L = 39.9$ mm).**

using the parallel model for gas/solid conduction interaction was applied to a 39.9-mm-thick fibrous insulation sample with a density of 48 kg/m$^3$ and with hot and cold boundary temperatures of 1293 and 293 K, respectively. The spatial variation of the ratio of steady-state radiative and conductive fluxes to the total heat flux throughout the thickness of fibrous insulation for pressures of $1.333 \times 10^{-5}$, 0.133, and 101.32 kPa are shown in Figs. 11a, 11b, and 11c, respectively. Nondimensional distances $x/L$ of zero and one represent the hot and cold boundaries, respectively. At a pressure of $1.333 \times 10^{-5}$ kPa (Fig. 11a), radiation is the dominant mode of heat

transfer. Conduction is negligible for $x/L$ up to 0.5, and then gradually increases to $q/q_T = 0.19$ at the cold boundary. At a pressure of 0.133 kPa (Fig. 11b), radiation is again the dominant mode of heat transfer at the hot boundary, and its relative magnitude decreases with increasing distance from the hot boundary. At $x/L = 0.83$ radiation and conduction fluxes are equal. Gas conduction is the dominant mode of heat transfer in the range $0.83 \leq x/L \leq 1$. The same general trends are observed at a pressure of 101.32 kPa (Fig. 11c), with radiation and conduction fluxes being equal at $x/L = 0.54$. As the pressure increases, the magnitude of the conduction heat flux increases throughout the whole domain, with the location where conduction flux surpasses the radiation flux moving closer to the insulation midplane from the cold boundary. The radiative flux is smaller at the hot boundary compared to the adjacent medium in Figs. (11b) and (11c) because conduction forces the material temperature in the vicinity of the wall to equal the wall temperature, thereby reducing the radiative heat flux.[31]

**Verification of Numerical Model: Transient Results**

A transient thermal test was conducted with fibrous insulation sample 10. The measured temporal variations of the chamber pressure and of the Inconel panel temperature that were achieved in simulating reentry conditions are shown in Figs. 12 and 13, respectively, along with the expected pressure and radiation equilibrium temperature histories corresponding to the reentry flight profile shown in Fig. 4. The measured pressures followed the expected flight pressure profile closely with the exception of elapsed time less than 300 s, where the measured pressures were higher than the expected reentry flight profile pressures. The agreement between the measured temperatures and the expected reentry flight profile temperatures was good until 2300 s, after which the measured temperatures deviated significantly from the expected flight profile. These differences were caused by the high convective cooling rates for the expected flight profile at lower altitudes and subsonic speeds that could not be duplicated in the ground-test vacuum chamber with passive cooling. The time variation of the measured temperatures on the water-cooled plate is shown in Fig. 14.

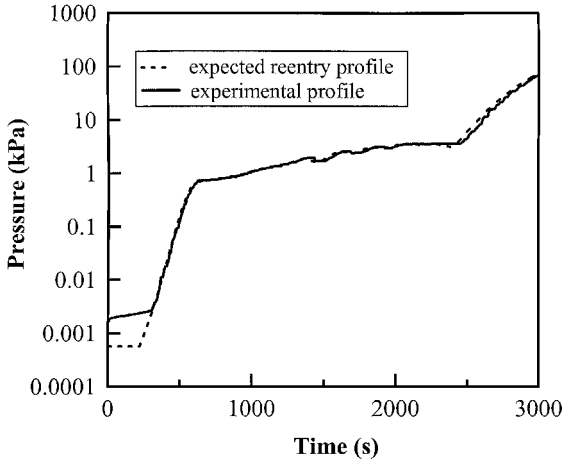


**Fig. 12 Comparison of expected flight pressure history with ground-test measured pressure history.**

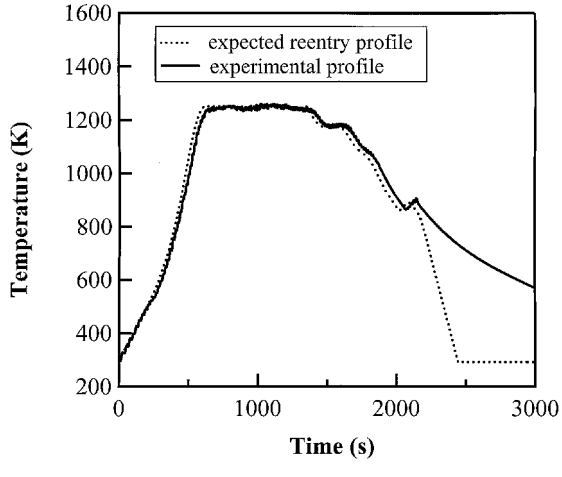


**Fig. 13 Comparison of ground-test measured Inconel panel temperature with expected reentry radiation equilibrium temperature.**

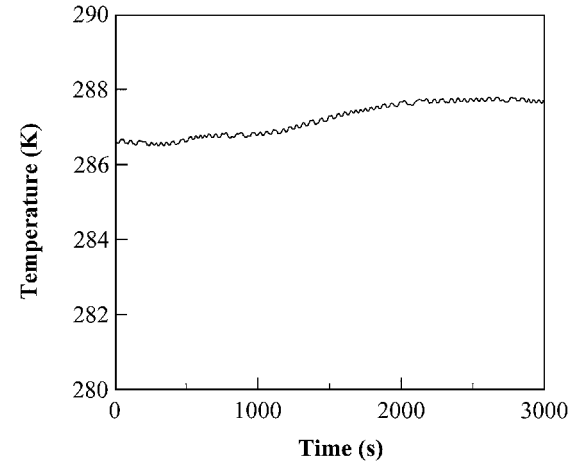


**Fig. 14 Ground test-measured variation of water-cooled plate temperature.**

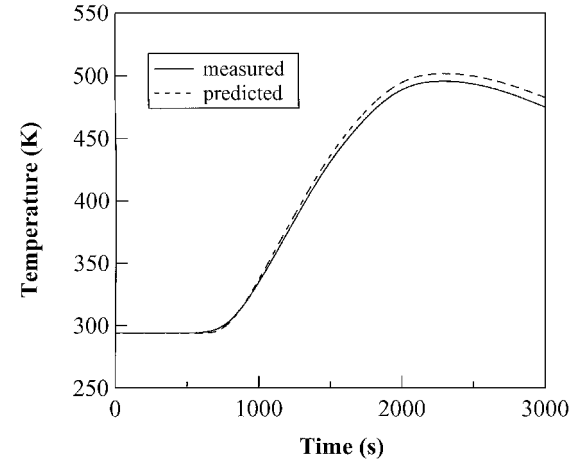


**Fig. 15 Comparison of predicted and ground-test measured aluminum panel temperatures.**

In simulating the ground test using the numerical model, the measured temporal variations of the Inconel panel and water-cooled plate temperatures from Figs. 13 and 14 were used for the boundary conditions, and the measured pressure values from Fig. 12 were used for gas conduction calculations. The parallel gas/solid conduction interaction model given in Eq. (17a) was used. The predicted temperature of the aluminum panel located between fibrous insulation samples with thicknesses of 53.3 and 13.3 mm shown in Fig. 2 was used for verification purposes. The temporal variations of the predicted and measured aluminum panel temperatures are shown in Fig. 15. The maximum difference between the numerically predicted and ground-test measured temperatures was 8 K, with a rms deviation of 4.8 K. The temporal variation of the relative difference between predicted and ground-test measured aluminum panel temperatures is shown in Fig. 16. The maximum difference was 1.6%, whereas the difference did not exceed 1.2% for elapsed times less than or equal to 2400 s. The close agreement between measured and predicted aluminum panel temperatures verified the numerical model for predicting the transient thermal performance of the fibrous insulation subject to conditions similar to an expected reentry aerodynamic heating profile.

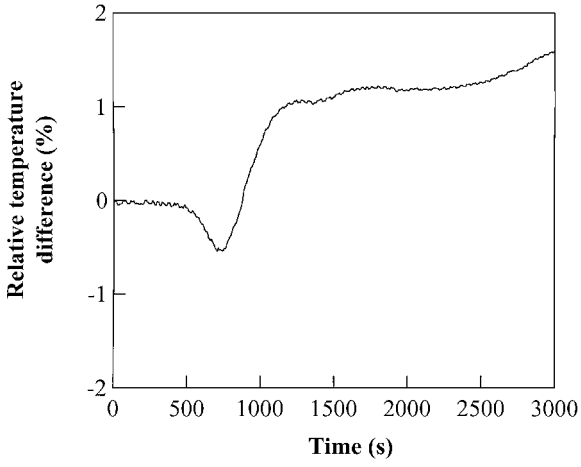


**Fig. 16 Relative difference between predicted and ground-test measured aluminum panel temperatures.**

In summary the numerical heat-transfer model was verified with both steady-state and transient thermal tests. The verification process was limited to thermal tests in a gaseous nitrogen environment and for the specific alumina fibrous insulation samples with a mean fiber strand diameter of $3 \times 10^{-6}$ m. The numerical heat-transfer model can be utilized to predict the heat transfer in the fibrous insulation in any gaseous medium by simply employing the gaseous medium's thermal conductivity and gas collision diameter in Eqs. (12) and (14), respectively. Even though the numerical model can be used for any fiber diameter, the radiative properties predicted in this study are specific to the fiber type and fiber diameter used, and new experiments have to be conducted to obtain estimated radiative properties for fibers of different material and diameter.

## Conclusions

The effective thermal conductivity of alumina fibrous insulations with densities of 24, 48, and 72 kg/m$^3$ and thicknesses of 13.3, 26.6, and 39.9 mm was measured over a pressure range of $1.33 \times 10^{-5}$–101.2 kPa and subject to temperature differences of 100–1000 K maintained across the sample thickness. The fibrous insulation samples with a density of 24 kg/m$^3$ and thicknesses of 26.6 and 39.9 mm were tested with two different heating orientations to investigate natural convection effects: applied heat flux aligned or opposite to the gravity vector. For fibrous insulation samples with densities equal to or larger than 24 kg/m$^3$, natural convection was not present as a mode of heat transfer. A transient test simulating reentry aerodynamic heating conditions was also performed.

A numerical model was developed for modeling combined radiation/conduction heat transfer in high-porosity, high-temperature fibrous insulation. The radiation heat transfer was modeled using a modified two-flux formulation assuming anisotropic scattering and gray media. The parallel model and Bhattacharyya's model[7] were investigated for modeling gas/solid conduction interaction. A genetic-algorithm parameter estimation technique was utilized in conjunction with measured effective thermal conductivities for fibrous insulation sample with a density of 24 kg/m$^3$ and at nominal pressures of $1.33 \times 10^{-4}$ and 99.98 kPa to obtain the best fit for the unknown radiation and conduction parameters needed in the numerical solution. The differences between predicted and measured effective thermal conductivities for all of the samples were typically within the $\pm 7.5\%$ experimental uncertainty range. The two models used for modeling gas/solid conduction interaction yielded similar results.

The numerical heat-transfer model was applied to the transient thermal test simulating reentry aerodynamic heating conditions. The maximum relative difference between the numerically predicted and ground-test measured temperatures on the aluminum panel, representing a launch vehicle structure, was 1.6%. The close agreement between measured and predicted aluminum panel temperatures verified the numerical model for predicting the transient thermal performance of the fibrous insulation subject to conditions similar to an expected reentry aerodynamic heating profile.

## Acknowledgments

The author thanks the following NASA Langley Research Center employees for their invaluable support: Wayne D. Geouge for fabrication and instrumentation of the test apparatus, Jeffrey R. Knutson for providing temperature and pressure controls for the tests and assisting in running the experiments, and Max L. Blosser for his guidance.

## References

[1] Blosser, M. L., Chen, R. R., Schmidt, I. H., Dorsey, J. T., Poteet, C. C., and Bird, R. K., "Advanced Metallic Thermal Protection System Development," AIAA Paper 2002-0504, Jan. 2002.

[2] Lee, S.-C., and Cunnington, G. R., "Conduction and Radiation Heat Transfer in High-Porosity Fiber Thermal Insulation," *Journal of Thermophysics and Heat Transfer*, Vol. 14, No. 2, 2000, pp. 121–136.

[3] Verschoor, J. D., and Greebler, P., "Heat Transfer by Gas Conduction and Radiation in Fibrous Insulations," *Transactions of the American Society of Mechanical Engineers*, Vol. 74, Aug. 1952, pp. 961–968.

[4] Hager, N. E., Jr., and Steere, R. C., "Radiant Heat Transfer in Fibrous Thermal Insulation," *Journal of Applied Physics*, Vol. 38, No. 12, 1967, pp. 4663–4668.

[5] Bankvall, C., "Heat Transfer in Fibrous Materials," *Journal of Testing and Evaluation*, Vol. 1, No. 3, 1973, pp. 235–243.

[6] Pawel, R. E., McElroy, D. L., Weaver, F. J., and Graves, R. S., "High Temperature Thermal Conductivity of a Fibrous Alumina Ceramic," *Thermal Conductivity*, edited by D. W. Yarbrough, Vol. 19, Plenum, New York, 1985, pp. 301–313.

[7] Bhattacharyya, R. K., "Heat-Transfer Model for Fibrous Insulations," *Thermal Insulation Performance*, edited by D. L. McElroy and R. P. Tye, ASTM Special Technical Publication 718, American Society for Testing and Materials, Philadelphia, 1980, pp. 272–286.

[8] Larkin, B. K., and Churchill, S. W., "Heat Transfer by Radiation Through Porous Insulations," *American Institute of Chemical Engineers Journal*, Vol. 5, No. 4, 1959, pp. 467–474.

[9] Tong, T. W., and Tien, C. L., "Radiative Heat Transfer in Fibrous Insulations-Part I: Analytical Study," *Journal of Heat Transfer*, Vol. 105, No. 1, 1983, pp. 70–75.

[10] Tong, T. W., Yang, Q. S., and Tien, C. L., "Radiative Heat Transfer in Fibrous Insulations-Part II: Experimental Study," *Journal of Heat Transfer*, Vol. 105, No. 1, 1983, pp. 76–81.

[11] Daryabeigi, K., "Analysis and Testing of High Temperature Fibrous Insulation for Reusable Launch Vehicles," AIAA Paper 99-1044, Jan. 1999.

[12] Daryabeigi, K., "Thermal Analysis and Design Optimization of Multilayer Insulation for Reentry Aerodynamic Heating," *Journal of Spacecraft and Rockets*, Vol. 39, No. 4, 2002, pp. 509–514.

[13] Daryabeigi, K., "Design of High Temperature Multi-layer Insulation for Reusable Launch Vehicles," Ph.D. Dissertation, Mechanical and Aerospace Engineering Dept., Univ. of Virginia, Charlottesville, VA, May 2000.

[14] Stark, C., and Fricke, J., "Improved Heat-Transfer Models for Fibrous Insulations," *International Journal of Heat and Mass Transfer*, Vol. 36, No. 3, 1993, pp. 617–625.

[15] Daryabeigi, K., "Effective Thermal Conductivity of High Temperature Insulations for Reusable Launch Vehicles," NASA TM-1999-208972, Feb. 1999.

[16] "Standard Test Method for Thermal Conductivity of Refractories," *Annual Book of ASTM Standards*, Vol. 15.01, American Society for Testing and Materials, West Conshohocken, PA, 2000, pp. 54–59.

[17] Ko, W. L., Quinn, R. D., and Gong, L., "Finite-Element Reentry Heat-Transfer Analysis of Space Shuttle Orbiter," NASA TP-2657, Dec. 1986.

[18] Blosser, M. L., "Investigation of Fundamental Modeling and Thermal Performance Issues for a Metallic Thermal Protection System Design," AIAA Paper 2002-0503, Jan. 2002.

[19] *Access to Space Study-Advanced Technology Team (Option 3) Design Handbook*, Vol. 3, NASA, Washington, DC, July 1993.

[20] Hender, D. R., "A Miniature Version of the JA-70 Aerodynamic Heating Computer Program, H800 (MINIVER)," McDonnell Douglas Astronautics, Rept. G0462, Huntington Beach, CA, June 1970.

[21] Thornton, E. A., *Thermal Structures for Aerospace Applications*, AIAA, Reston, VA, 1996, p. 18.

[22] Sparrow, E. M., and Cess, R. D., *Radiation Heat Transfer*, augmented ed., McGraw–Hill, New York, 1978, pp. 255–271.

[23] Domoto, G. A., and Wang, W. C., "Radiative Transfer in Homogeneous Nongray Gases with Nonisotropic Particle Scattering," *Journal of Heat Transfer*, Vol. 96, No. 3, 1974, pp. 385–390.

[24]Matthews, L. K., Viskanta, R., and Incropera, F. P., "Combined Conduction and Radiation Heat Transfer in Porous Materials Heated by Intense Solar Radiation," *Journal of Solar Energy Engineering*, Vol. 107, No. 1, 1985, pp. 29–34.

[25]Siegel, R., and Howell, J. R., *Thermal Radiation Heat Transfer*, 2nd ed., McGraw–Hill, New York, 1981, pp. 426, 427.

[26]Marschall, J., Maddren, J., and Parks, J., "Internal Radiation Transport and Effective Thermal Conductivity of Fibrous Ceramic Insulation," AIAA Paper 2001-2822, June 2001.

[27]Gebhart, B., *Heat Conduction and Mass Diffusion*, McGraw–Hill, New York, 1993, pp. 442–444.

[28]Williams, S. D., and Curry, D. M., "Prediction of Rigid Silica Based Insulation Conductivity," NASA TP-3276, Jan. 1993.

[29]Haupt, R. L., and Haupt, S. E., *Practical Genetic Algorithms*, Wiley, New York, 1998.

[30]Garcia, S., Guynn, J., and Scott, E. P., "Use of Genetic Algorithms in Thermal Property Estimation: Part II—Simultaneous Estimation of Thermal Properties," *Numerical Heat Transfer*, Vol. 33, No. 2, 1998, pp. 149–168.

[31]Viskanta, R., "Heat Transfer by Conduction and Radiation in Absorbing and Scattering Materials," *Journal of Heat Transfer*, Vol. 87, No. 1, 1965, pp. 143–150.